



[JOURNAL HOME \(/OE/HOME.CFM\)](#)

[ABOUT \(/OE/JOURNALS/ABOUT.CFM\)](#)

[ISSUES IN PROGRESS \(/OE/UPCOMINGISSUE.CFM\)](#)

[CURRENT ISSUE \(/OE/ISSUE.CFM\)](#)

[ALL ISSUES \(/OE/BROWSE.CFM\)](#)

[FEATURE ISSUES \(/OE/FEATURE.CFM\)](#)

Figures (9)

Data Availability

Equations (26)

References (34)

Cited By (1)

Optics Express

Vol. 29, Issue 20 (/oe/issue.cfm?volume=29&issue=20), pp. 31549-31560 (2021)

• <https://doi.org/10.1364/OE.439449> (<https://doi.org/10.1364/OE.439449>)

Metrics

[Back to Top](#)

Investigation of the effective aperture: towards high-resolution Fresnel incoherent correlation holography

Fengying Ma, Yu Li, Xi Wang, Yanli Du, Qiaoxia Gong, Jingkai Cheng, Li Qin, Jianpo Su, and Yongsheng Hu

Open Access

PDF Article

(<viewmedia.cfm?uri=oe-29-20-31549&seq=0>)

Abstract

Fresnel incoherent correlation holography (FINCH) shows great advantages of coherent-light-source-free, high lateral resolution, no scanning, and easy integration, and has exhibited great potential in recording three-dimensional information of objects. Despite the rapid advances in the resolution of the FINCH system, little attention has been paid to the influence of the effective aperture of the system. Here, the effective aperture of the point spread function (PSF) has been investigated both theoretically and experimentally. It is found that the effective aperture is mainly restricted by the aperture of the charge-coupled device (CCD), the pixel size of the CCD, and the actual aperture of the PSF at different recording distances. It is also found that the optimal spatial resolution exists only for a small range of recording distance, while this range would become smaller as the imaging wavelength gets longer, leading to the result that the optimal spatial resolution is solely determined by the actual aperture of the PSF. By further combining the FINCH system with a microscopy system and optimizing the recording distance, a spatial resolution as high as 0.78 μm at the wavelength of 633 nm has been obtained, enabling a much higher quality imaging of unstained living biological cells compared to the commercial optical microscope. The results of this work may provide some helpful insights into the design of high-resolution FINCH systems and pave the way for their application in biomedical imaging.

© 2021 Optical Society of America under the terms of the OSA Open Access Publishing Agreement
 (https://doi.org/10.1364/OA_License_v1#VOR-OA) **Article Outline** 

1. Introduction

Incoherent digital holography is a promising three-dimensional optical recording technology. Investigation of the effective aperture of the holography to use light sources with a wide bandwidth, thus eliminating the demand for a stable optical setup in common coherent digital holography [1,2]. Till now, various kinds of incoherent digital holography have been investigated [3–12] and have been widely used in the areas such as fluorescence microscopy imaging [13–15], color holography [16,17], aberration compensation in adaptive optics [18] and spiral phase contrast imaging [19,20]. Among them, Fresnel incoherent correlation holography (FINCH) [3] is an in-line, single-channel path interferometer that contains a spatial light modulator (SLM) and a charge-coupled device (CCD). The SLM acts as both a beam splitter and a phase shifter. The incident beam emitted from a single-point object is modulated by the SLM and split into two beams which interfere with each other to form a Fresnel zone plate-like hologram, called point spread function (PSF) [21], at the surface of the CCD. The summation of all the PSFs created by each point source gives the hologram of a spatially incoherent object. Comparing with other incoherent holographic techniques [22], the FINCH system shows many potential advantages such as high resolution which is beyond the Rayleigh diffraction limit [23], no time and space scanning so that a high imaging speed could be attained, and easy to match with existing optical systems [19,24,25,26]. During the past decade, many efforts including adopting synthetic aperture [27,28], polarization multiplexing [29,30], dual lenses multiplexing on SLM [31], structured illumination [32], and using a glass lens and a liquid crystal gradient index (GRIN) lens to replace the SLM [33], have been made to improve the resolution of the FINCH system. However, the factors that influence the spatial resolution of the system have not been fully explored. It is generally known that the effective aperture of the PSF is an essential factor that determines the spatial resolution of a FINCH system [30]. However, with the change of the recording distance, the effective aperture of the PSF might be determined by its own aperture size, the CCD aperture, or the CCD pixel size. So far, collaborative analysis of the above factors on the spatial resolution of the system is still lacking.

In this paper, the factors that influence the spatial resolution of the dual-lens multiplexed FINCH system are systematically investigated. It is found that the effective aperture of the PSF could be constrained by the pixel size of the CCD, the aperture size of the CCD and the actual aperture of the PSF. Both theoretical analysis and experiment results for different recording distances have shown that the spatial resolution of the system depends mainly on the effective aperture related to the aperture of the PSF. Meanwhile, by combining it with a microscopy system and recording at an appropriate distance, a spatial resolution as high as 0.78 μm has been obtained for the FINCH system, enabling high-quality imaging of unstained living biological cells.


2. Theoretical analysis of the resolution for the dual-lens FINCH system

Figure 1 shows the schematic of the dual-lens FINCH system. A point source located at $(x_s, y_s, -z_s)$ induces a diverging spherical wave on the lens L with the form:

$$E_L = \exp\{i\pi(z_s\lambda)^{-1}[(x-x_s)^2 + (y-y_s)^2]\}.$$

 (viewmedia.cfm?ur

Article Outline


 (mailto:?subject=Ai

Optics Express:%0AFer

where λ is the working wavelength. The spherical wave passes through the lens L (with the focal length of f_0) and propagates a distance d to the SLM, the complex amplitude on the SLM plane can be expressed as:

Figures (9)

Data Availability

Equations (26)

References (34)

Cited By (1)

Metrics

Back to Top

$$E_{SLM} = \exp\{i\pi[(f_e + d)\lambda]^{-1}[(x - f_e x_s / z_s)^2 + (y - f_e y_s / z_s)^2]\},$$

here $1 / f_e = 1 / z_s - 1 / f_0$. Right after the SLM, with the reflection function of

$$R(x, y) = B \exp[-i\pi(\lambda f_{d1})^{-1}(x^2 + y^2) + i\theta] \\ + B' \exp[-i\pi(\lambda f_{d2})^{-1}(x^2 + y^2)],$$

where B and B' are constants, θ is the phase constant, f_{d1} and f_{d2} are the focal lengths of the two diffractive lenses loaded on the SLM. The spherical wave continues to propagate a distance z_h and finally reaches the surface of the CCD. The complex amplitude at the surface of the CCD is as follows:

$$E_{CCD} = B \exp\left\{\frac{i\pi}{\lambda(f_1 + z_h)} \left[\left(x - \frac{f_1 f_e}{z_s(f_e + d)} x_s\right)^2 + \left(y - \frac{f_1 f_e}{z_s(f_e + d)} y_s\right)^2 \right] + i\theta\right\} \\ + B' \exp\left\{\frac{i\pi}{\lambda(f_2 + z_h)} \left[\left(x - \frac{f_2 f_e}{z_s(f_e + d)} x_s\right)^2 + \left(y - \frac{f_2 f_e}{z_s(f_e + d)} y_s\right)^2 \right]\right\},$$

here $1 / f_{1,2} = 1 / (f_e + d) - 1 / f_{d1,2}$. The intensity distribution on the surface of the CCD is the so-called PSF, which can be expressed as:

$$I_{\text{psf}}(x, y) = C + C_1 \exp\left\{\frac{-i\pi}{\lambda z_T} [(x - M_T x_s)^2 + (y - M_T y_s)^2] - i\theta\right\} + c. c. ,$$

here $C = B + B'$, $C_1 = B + B'$, $c.c.$ is the complex conjugate of the second term on the right, M_T is the lateral magnification of this system which equals $z_h f_e / [z_h (f_e + z_h) + z_r]$ and z_r is the reconstruction distance which satisfies $1 / z_r = 1 / (f_1 + z_h) - 1 / (f_2 + z_h)$. Using a common computation routine of phase-stepping [19], three different PSFs with different phase shifts are captured and superimposed in the computer, then the complex hologram free of the twin image and zero-order image can be obtained with the form

$$H_F(x, y) = A \exp \left\{ \frac{-i\pi}{\lambda z_r} [(x - M_T x_s)^2 + (y - M_T y_s)^2] \right\},$$

here A is a complex constant. The image of the point source can be reconstructed from H_F by Fresnel propagation [19] as

$$S(x, y) = P(x, y) H_F(x, y) * \exp \left[\frac{i\pi}{\lambda z_r} (x^2 + y^2) \right].$$

where the asterisk denotes a two-dimensional convolution. $P(x, y)$ is an aperture function determined by the effective aperture of the PSF. This image is actually the reconstructed image of a point source whose distribution determines the spatial resolution of the system [23,30,31]. From formula (6), we can see that the complex hologram is essentially a convergent spherical wave, and the reconstructed image obtained by formula (7) is the diffraction pattern of the convergent spherical wave on the aperture. The corresponding radius of the Airy spot is

$$r_0 = \frac{0.61 \lambda z_r}{R_{\text{eff}}}.$$

where R_{eff} is the effective radius of the PSF. According to the Rayleigh criterion and considering the lateral magnification of the system, the spatial resolution of the system can be then obtained as:

$$\sigma = \frac{0.61 \lambda z_r}{M_T R_{\text{eff}}}.$$

Article Outline



(viewmedia.cfm?ur

(mailto:?subject=Ar

Optics Express:%0AFer

"Investigation of the ef

31549-31560 (2021)%0

-----%0AThis i



Thus, R_{eff} is the key parameter to determine the spatial resolution of the system.

Figures (9)

Data Availability

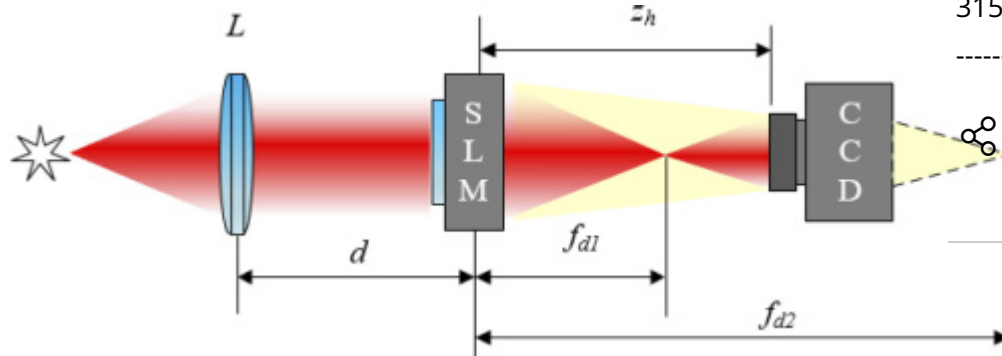


Fig. 1. Schematics of dual-lens FINCH. L: collimating lens; SLM: spatial light modulator; CCD: charge-coupled device.

Download Full Size (/viewmedia.cfm?uri=oe-29-20-31549&figure=oe-29-20-31549-g001&imagetype=full) | PPT Slide (/viewmedia.cfm?uri=oe-29-20-31549&figure=oe-29-20-31549-g001&imagetype=pwr) | PDF (/viewmedia.cfm?uri=oe-29-20-31549&figure=oe-29-20-31549-g001&imagetype=pdf)

To better understand the R_{eff} , the following equation is defined:

$$R_{\text{eff}} = \min \{R_p, R_{\text{CCD}}, R_{\text{CO}}\},$$

here R_p , R_{CCD} and R_{CO} are the radii of the PSF, which are determined by the pixel size of the CCD, the aperture size of the CCD, and the actual size of the PSF, respectively. Hence, the spatial resolution of the system can be expressed as:

$$\Delta_{\min} = \max \left\{ \frac{0.61\lambda |z_T|}{M_T R_p}, \frac{0.61\lambda |z_T|}{M_T R_{\text{CCD}}}, \frac{0.61\lambda |z_T|}{M_T R_{\text{CO}}} \right\}.$$

In the following, we will deduce the factors that determine the R_p , R_{CCD} and R_{CO} , and correlate them with the optimal spatial resolution of the system.

2.1 R_p constrained by the pixel size of CCD

It is well known that the PSF has the form of a cosine Fresnel zone plate, which consists of a series of bright and dark concentric rings. As the radius increases, the circular rings become denser and denser. When the radius difference between the adjacent bright and dark fringes is smaller than the pixel size of the CCD, the CCD will be unable to identify the bright or dark fringes, and other outer rings cannot be recorded. Based on this assumption, the radius of the PSF determined by the pixel size of the CCD can be calculated as follows:

The PSF in Eq. (5) can be simplified to the following form:

$$I_{\text{psf}}(x, y; r_s, z_s) = C + 2C_1 \cos \left\{ \frac{\pi}{\lambda z_r} [(x - M_T x_s)^2 + (y - M_T y_s)^2] + \theta \right\},$$

Under the condition that

$$\frac{\pi}{\lambda z_r} [(x - M_T x_s)^2 + (y - M_T y_s)^2] + \theta = (2m - 1)\pi, \quad m = 0, 1, 2, 3 \dots$$


the stripes recorded on the CCD are dark rings. The above equation can be simplified into the following form:

$$r_1^2 = \frac{z_r \lambda [(2m - 1)\pi - \theta]}{\pi}, \quad m = 0, 1, 2, 3 \dots$$

Similarly, we can get the equation of the bright rings:

$$r_2^2 = \frac{z_r \lambda [2m\pi - \theta]}{\pi}, \quad m = 0, 1, 2, 3 \dots$$

Article Outline

 (viewmedia.cfm?ur

 (mailto:subject=Ar

Optics Express; %0AFer

"Investigation Base

31549-31560s (2021)%0

-----%0AThis i

Equations (26)

References (34)

Cited By (1)

Metrics

Back to Top



where r_1 and r_2 are the radii of the above dark and bright rings, respectively. The difference between Eq. (15) and Eq. (14) leads to the following equation:

$$r_2^2 - r_1^2 = \lambda z_r.$$

Data Availability

Equations (26)

References (34)

Cited By (1)

Metrics

Back to Top

$$\begin{cases} r_2 + r_1 = 2R_p \\ r_2 - r_1 = \delta_c \end{cases},$$

Based on the above assumptions, when two adjacent fine light lines and dark lines are simultaneously recorded by the same pixel on the CCD, the following equation can be obtained:

here δ_c is the pixel size of the CCD. Based on (16) and (17), the corresponding radius R_p can be calculated to be

$$R_p = \frac{\lambda z_r}{2\delta_c}.$$

As can be seen, R_p is not only inversely proportional to δ_c , but also closely related to the imaging wavelength and the reconstruction distance.

2.2 R_{CCD} constrained by the aperture size of CCD

Since the PSF can not exceed the aperture size of the CCD, when assuming that the photosensitive area of the CCD is square and the numbers of pixels in both horizontal and vertical directions are the same, R_{CCD} can be calculated to be

$$R_{\text{CCD}} = \frac{N\delta_c}{2},$$

here N is the number of pixels in the horizontal or vertical direction.

2.3 R_{CO} constrained by the actual aperture of the PSF

Figure 2 shows the actual aperture of the PSF for the dual lens FINCH system at different recording distances. Under the condition of perfect overlap of the two beam cones, the distance between the SLM and the CCD is given by $2 f_{d1} f_{d2} / (f_{d1} + f_{d2})$ [31]. Based on the triangular similarity, we can obtain that

$$R_{CO} = \begin{cases} \frac{R_{SLM}}{f_{d1}} |f_{d1} - z_h| z_h \leq \frac{2f_{d1}f_{d2}}{f_{d1} + f_{d2}} \\ \frac{R_{SLM}}{f_{d2}} |f_{d2} - z_h| z_h > \frac{2f_{d1}f_{d2}}{f_{d1} + f_{d2}} \end{cases}$$

Based on the above discussion, and considering that the two lenses with similar focal length are usually used in FINCH system [31], we assume that $\Delta f = f_{d2} - f_{d1} \ll f_{d1,2}$, $f_{d1} < f_{d2}$, $R_{CCD} < R_{SLM}$, $z_s = f_0$, then $f_e \rightarrow \infty$, $f_{1,2} = -f_{d1,2}$. In order to determine the effective aperture of the PSF, we have to consider the influence of the recording distance (z_h) on R_P , R_{CCD} and R_{CO} . This leads to 7 sorting regions along the recording distance determined by Eqs. (21)–(26). As shown in Fig. 3. For regions ① and ⑦, R_{eff} is determined by R_{CCD} , and for regions ②, ③, ⑤ and ⑥, R_{eff} is determined by R_{CO} , and for region ④, R_{eff} is determined by R_P . It should be noted that the width of the regions ②, ③, ④, ⑤ and ⑥ is also related to the imaging wavelength λ according to Eqs. (22)–(25). With the increase of λ , the regions ③, ④ and ⑤ all shrink towards the center P where the optimal spatial resolution is located. Therefore, there is a critical wavelength; when the wavelength increases to the critical wavelength, P_3 and P_4 will coincide at the point P , and the region ④ will disappear. For wavelength longer than the critical wavelength, the spatial resolution is only related to R_{CO} for the recording distances from P_1 to P_6 , which means $R_{eff} = R_{CO}$.

$$P_1 = f_{d1} - (R_{CCD}f_{d1})/R_{SLM},$$

$$P_2 = \left[(f_{d1} + f_{d2}) - \sqrt{(f_{d2} - f_{d1})^2 + 8\delta_c R_{CCD}(f_{d2} - f_{d1})/\lambda} \right] / 2,$$

$$P_3 = f_{d2} - 2\delta_c R_{SLM}(f_{d2} - f_{d1})/\lambda f_{d1},$$

Article Outline

$$P_4 = f_{d1} + 2\delta_c R_{\text{SLM}}(f_{d2} - f_{d1})/\lambda f_{d2},$$

FIGURES (9)

Data Availability

Equations (26)

$$P_5 = \left[(f_{d1} + f_{d2}) + \sqrt{(f_{d2} - f_{d1})^2 + \left(\frac{R_{\text{CCD}}}{R_{\text{SLM}}} \right)^2} \right] / 2,$$

Cited By (1)

Metrics

Back to Top

$$P_6 = f_{d2} + (R_{\text{CCD}} f_{d2}) / R_{\text{SLM}}$$

(viewmedia.cfm?ur

(mailto:?subject=Ar

Optics Express:%0AFer

"Investigation of the ef

31549-31560 (2021)%0

-----%0AThis i

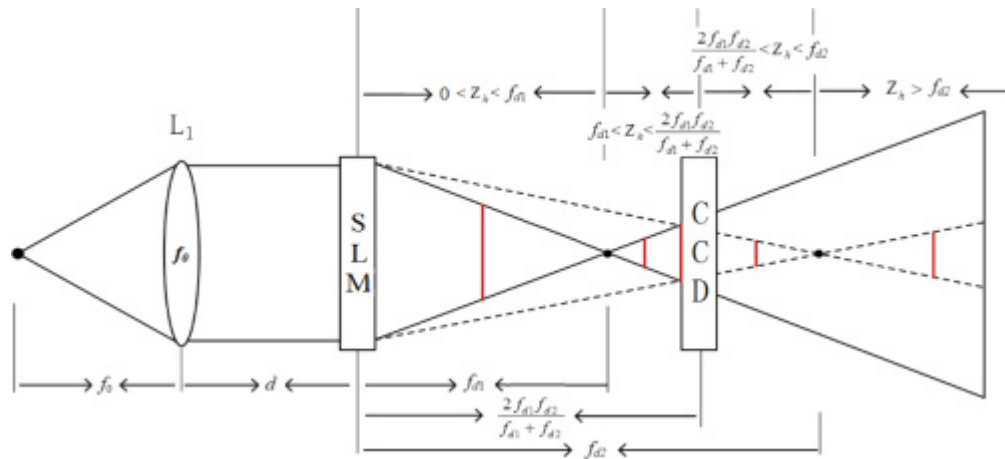
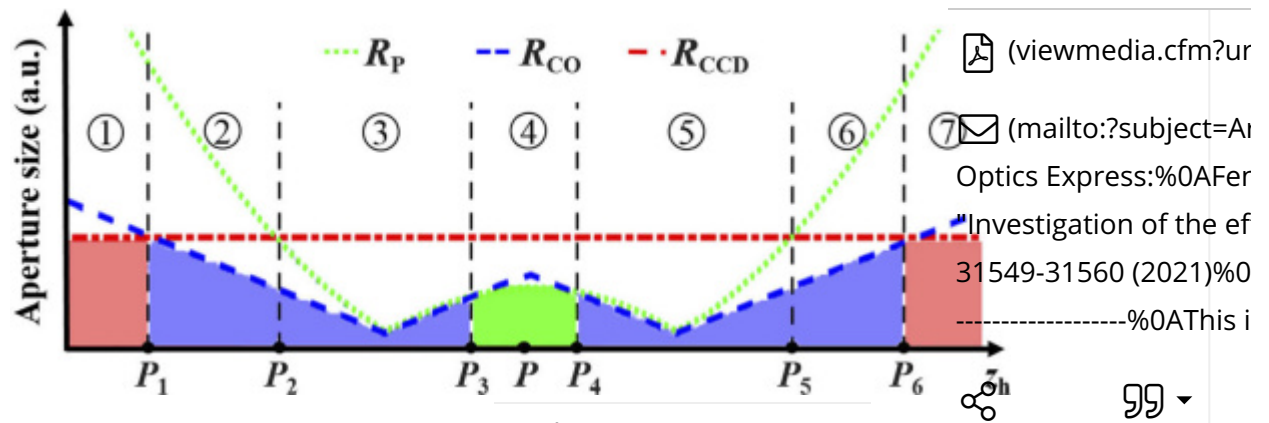


Fig. 2. The schematic of the actual aperture of the PSF at different z_h (denoted by the red line).

Download Full Size (/viewmedia.cfm?uri=oe-29-20-31549&figure=oe-29-20-31549-g002&imagetype=full) | PPT Slide (/viewmedia.cfm?uri=oe-29-20-31549&figure=oe-29-20-31549-g002&imagetype=pwr) | PDF (/viewmedia.cfm?uri=oe-29-20-31549&figure=oe-29-20-31549-g002&imagetype=pdf)



Cited By (1)

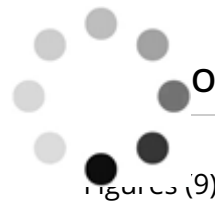
Fig. 3. Aperture size of R_P , R_{CCD} and R_{CO} at different recording distances.

Download Full Size (/viewmedia.cfm?uri=oe-29-20-31549&figure=oe-29-20-31549-g003&imagedtype=full) | PPT Slide (/viewmedia.cfm?uri=oe-29-20-31549&figure=oe-29-20-31549-g003&imagedtype=pwr) | PDF (/viewmedia.cfm?uri=oe-29-20-31549&figure=oe-29-20-31549-g003&imagedtype=pdf)

In this section, we have systematically analyzed the effective aperture of the system, which is related to the pixel size of the CCD, the aperture size of CCD, and the actual aperture of the PSF (R_P , R_{CCD} and R_{CO}). Specifically, the influence of the recording distance has been discussed. In the following, we will try to elucidate the influence of the above factors experimentally.

3. Experimental results

The experimental setup of the FINCH system is shown in Fig. 4. The incoherent light source is a Xenon lamp (CEL-TCX250, 250W). BF is a bandpass filter with a peak wavelength of either 633 nm or 500 nm and a bandwidth (full width at half maximum) of 20 nm. The tested object is a USAF1951 resolution target. The SLM is phase-only (Holo-eye Pluto, 1920×1080 pixels, 8 μm pixel pitch), f_{d1} and f_{d2} are 245 mm and 255 mm, respectively. The focal length of L_1 is fixed at 60 mm while a value of either 250 mm or 100 mm is used for L_2 . BS_1 and BS_2 are the beam splitter cubes. The distance between the collimating lens L_2 and the SLM is $d = 130$ mm. The polarization of the polarizer is adjusted to the direction specified by the SLM. The CCD (Q-IMAGING digital camera RETIGA 6000, pixel size $\delta_c = 4.54$ μm) has 2750×2200 pixels. For the convenience of subsequent processing, we use only 2048×2048 pixels here. Under these experimental conditions, P_3 will coincide with P_4 at a critical wavelength of 312.2 nm. Therefore, we speculate that the spatial resolution of the system is independent of R_P in the whole visible wavelength range. In the first group of the experiment, the imaging wavelength is 633 nm. The focal length of the collimating lens L_2 is 100 mm, corresponding to a magnification M_T of 2.5, and the test object is placed on the front focal plane of L_2 . We can calculate that $P_1 = -18.6$ mm, $P_2 = 223.7$ mm, $P_3 = 252.4$ mm, $P_4 = 247.4$ mm, $P_5 = 276.3$ mm, and $P_6 = 529.5$ mm. Since $P_3 > P_4$, the spatial resolution of the system is no longer determined by R_P , but only related to R_{CO} for a wide range of recording distances, for instance, from P_2 to P_5 .



Outline



(viewmedia.cfm?ur

(mailto:?subject=Ar

Optics Express:%0AFer

"Investigation of the ef

31549231560(2021)%0

-----%0AThis i

PPT Slide

Fig. 4. Schematic of the FINCH system. L₁, L₂: Lens; P: Polarizer; BF: Bandpass filter; BS: Beam splitter.

Download Full Size (/viewmedia.cfm?uri=oe-29-20-31549&figure=oe-29-20-31549-g004&imagetype=full) | PPT Slide (/viewmedia.cfm?uri=oe-29-20-31549&figure=oe-29-20-31549-g004&imagetype=pwr) | PDF (/viewmedia.cfm?uri=oe-29-20-31549&figure=oe-29-20-31549-g004&imagetype=pdf)

Data Availability

Equations (26)

References (34)

Cited By (1)

Metrics

[Back to Top](#)

Figure 5 shows the reconstructed images of the USAF1951 resolution target at different recording distances from 230 mm to 270 mm with an interval of 5 mm. According to Eqs. (9) and (20), the spatial resolution of the system is best when the record distance satisfies the condition of $z_h = 2 f_{d1} f_{d2} / (f_{d1} + f_{d2})$, which corresponds to Fig. 5(e), with a recording distance of 250 mm.



Fig. 5. Reconstructed images of the USAF1951 resolution target at recording distances from 230 mm to 270 mm, with an interval of 5 mm. The imaging wavelength is 633 nm, and the focal length of L₂ is 100 mm.

Download Full Size (/viewmedia.cfm?uri=oe-29-20-31549&figure=oe-29-20-31549-g005&imagetype=full) | PPT Slide (/viewmedia.cfm?uri=oe-29-20-31549&figure=oe-29-20-31549-g005&imagetype=pwr) | PDF (/viewmedia.cfm?uri=oe-29-20-31549&figure=oe-29-20-31549-g005&imagetype=pdf)

In Fig. 5(e), the fifth unit of the sixth group can be distinguished, with the corresponding spatial resolution of 4.92 μm, which is consistent with the value (4.47 μm) estimated by R_{CO} . In contrast, the spatial resolution values calculated by R_{CCD} and R_P are 0.08 μm and 2.22 μm, respectively, which deviate greatly from the experimental results. These results coincide well with the above analysis of spatial resolution of the system.

To make a quantitative comparison for the results in Fig. 5, Fig. 6 presents the visibility of the sixth unit of the fourth group for the reconstructed images in Fig. 5. The visibility is defined as $(I_{max} - I_{min}) / (I_{max} + I_{min})$, which is a standard quantity used to characterize the resolution [23]. The visibility first increases and then decreases with the increase of the recording distance and reaches the maximum of 0.57 when the recording distance is 250 mm, which is corresponding to the recording distance $z_h = 2 f_{d1} f_{d2} / (f_{d1} + f_{d2})$.

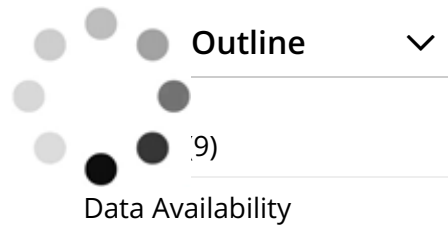


Fig. 6. The visibility of the sixth unit of the fourth group for the reconstructed images in Fig. 5. [Download Full Size \(/viewmedia.cfm?uri=oe-29-20-31549&figure=oe-29-20-31549-g006&imagetype=full\)](#) | [PPT Slide \(/viewmedia.cfm?uri=oe-29-20-31549&figure=oe-29-20-31549-g006&imagetype=pwr\)](#) | [PDF \(/viewmedia.cfm?uri=oe-29-20-31549&figure=oe-29-20-31549-g006&imagetype=pdf\)](#)

Metrics

To further verify our theoretical analysis, we performed a set of experiment with a different imaging wavelength of 500 nm and a focal length of 250 mm for L_2 . Other experimental parameters were kept the same as those in Fig. 5. Under these configuration parameters, $P_1=18.6$ mm, $P_2=220.5$ mm, $P_3=251.7$ mm, $P_4=248.1$ mm, $P_5=279.5$ mm, and $P_6=529.5$ mm. Figures 7(a)–(c) show the reconstructed images at the recording distances of 245 mm, 250 mm and 255 mm, respectively. The best spatial resolution is also obtained when the recording distance is $2 f_{d1} f_{d2} / (f_{d1} + f_{d2})$, as shown in Fig. 7(b), where the fifth unit of the fifth group can be distinguished, corresponding to a spatial resolution of 9.84 μm , which is consistent with the value (9.00 μm) estimated by R_{CO} and deviated greatly from the values estimated by R_{CCD} (0.16 μm) and R_p (5.54 μm). Again, the experimental results agree well with the above theoretical analysis of the spatial resolution of the system.



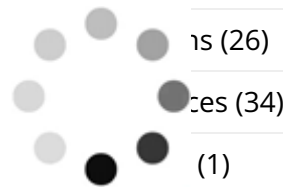
Fig. 7. Reconstructed images of the USAF1951 resolution target at recording distances of 245 mm, 250 mm, and 255 mm. The imaging wavelength is 500 nm, and the focal length of L_2 is 250 mm. [Download Full Size \(/viewmedia.cfm?uri=oe-29-20-31549&figure=oe-29-20-31549-g007&imagetype=full\)](#) | [PPT Slide \(/viewmedia.cfm?uri=oe-29-20-31549&figure=oe-29-20-31549-g007&imagetype=pwr\)](#) | [PDF \(/viewmedia.cfm?uri=oe-29-20-31549&figure=oe-29-20-31549-g007&imagetype=pdf\)](#)

Since the FINCH system is believed to be compatible with existing optical systems, we also study the microscopic imaging performance of the system. A 20 \times 0.4NA objective lens with a working distance of 5.9 mm is placed in front of the BS_1 (see Fig. 4) to form a FINCH-based microscopic imaging system. The objective lens plays the role of pre-magnification, and the image formed by it is on the front focal plane of L_2 . Figure 8 shows the microscopic imaging results of the resolution target at the best recording distance with the working wavelength of 633 nm. In Fig. 8(a), the third unit of the ninth group can be clearly

distinguished, corresponding to a spatial resolution of $0.78 \mu\text{m}$. Figure 8(b) shows the normalized intensity profiles of the corresponding area denoted by the red and blue lines in Fig. 8(a), which demonstrates clear intensity variation between the different vertical and horizontal bar patterns.

Figures (9)

Data Availability

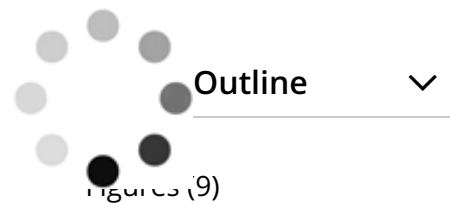


Metrics

Fig. 8. (a) Reconstructed image of the resolution target from the FINCH-based microscopic imaging system; (b) Normalized intensity profiles of the area from (a) depicted by the red and blue lines.

Download Full Size (/viewmedia.cfm?uri=oe-29-20-31549&figure=oe-29-20-31549-g008&imagetype=full) | PPT Slide (/viewmedia.cfm?uri=oe-29-20-31549&figure=oe-29-20-31549-g008&imagetype=pwr) | PDF (/viewmedia.cfm?uri=oe-29-20-31549&figure=oe-29-20-31549-g008&imagetype=pdf)

Due to the high spatial resolution of the microscope system, we further used it to image living biological cells. Figure 9(a) shows the microscopic imaging results of the unstained living oral epithelial cells. For comparison, the image captured by an optical microscope (Nikon Eclipse TS100) is also presented in Fig. 9(b). It can be seen that the FINCH microscope has higher spatial resolution under the same magnification. As shown in Figs. 9(c) and 9(d), the image from the FINCH microscope shows clearer boundary information and more legible information of the cell membranes and the cytoplasm. Although the brightness is inferior for the FINCH microscopic system, this could be circumvented by increasing the intensity of the light source or extending the exposure time. Meanwhile, the light source image in Fig. 9(a) could be also eliminated by using a light source with better uniformity. Figure 9(e) shows the phase of complex hologram corresponding to Fig. 9(a). It is worth mentioning that external aberrations such as misalignments are likely to cause little influence for current system. Intrinsically, the FINCH system is relatively simple so that the external aberrations are believed to be not as severe as classical holography. In fact, the key advantage of FINCH is that the object itself serves as the light source, enabling three-dimensional imaging from any object, either by reflection or emission of light such as fluorescence. Thus a coherent laser light source and the associated precise alignment of a reference and sample beam concomitant with classical holography are not needed [34]. In addition, during the experiment, we have carefully adjusted the system's optical path by using a He-Ne laser for collimation. We have also captured the image without the object as the background, which was later removed when captured the image of the object. This can further minimize the influence of the external aberrations, including the surface error of the optical elements in the system. Overall, the above results indicate that the FINCH system may have great potential application in the field of unlabeled biomedical imaging.


[\(viewmedia.cfm?ur](#)
[\(mailto:?subject=Ar](mailto:?subject=Ar)

Optics Express:%0AFer

"Investigation of the ef

Fig. 9. Picture of living cells of oral epithelium. (a) Recorded by the FINCH microscopic system; (b) Recorded by an optical microscope; (c) and (d) Magnified images of the areas with the red box in (a) and (b), respectively; (e) The phase of the complex hologram corresponding to (a). The scale bar is 50 μm .

Download Full Size (/viewmedia.cfm?uri=oe-29-20-31549&figure=oe-29-20-31549-g009&imagetype=full) | PPT Slide (/viewmedia.cfm?uri=oe-29-20-31549&figure=oe-29-20-31549-g009&imagetype=pwr) | PDF (/viewmedia.cfm?uri=oe-29-20-31549&figure=oe-29-20-31549-g009&imagetype=pdf)

[Back to Top](#)

4. Conclusion

In conclusion, we have investigated the factors that influence the spatial resolution of the dual-lens multiplexed FINCH system theoretically and experimentally. It is found that the effective aperture is mainly restricted by the aperture of the CCD, the pixel size of the CCD, and the actual aperture of the PSF at different recording distances. The optimal spatial resolution exists only for a small range of recording distance, while this range would become smaller as the imaging wavelength gets longer, leading to the result that the optimal spatial resolution is solely determined by the R_{CO} . By further combining the FINCH system with a microscopic system, a high spatial resolution of 0.78 μm at the wavelength of 633 nm has been achieved and be successfully used to image the unstained living oral epithelial cells, which shows more legible information of the cell membranes and a clearer view of cytoplasm compared with the traditional optical microscope. The results of this work may provide some helpful insights into the design of high-resolution FINCH systems and would pave the way for their application in biomedical imaging.

Funding

National Natural Science Foundation of China (11504333, 61307019, 61505178, 11904323).






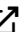
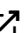




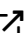

Disclosures

The authors declare no conflicts of interest.

Data availability

The raw data supporting this article's conclusions will be made available by the authors without undue reservation.

References

1. J. Rosen, A. Vijayakumar, M. Kumar, M. R. Rai, R. Kelner, Y. Kashter, A. Bulbul, and S. Mukherjee, "Recent advances in self-interference incoherent digital holography," *Appl. Opt.* **11**(1), 1–66 (2019). [CrossRef (<http://dx.doi.org/10.1364/AOP.11.000001>)] 
2. J. P. Liu, T. Tahara, Y. Hayasaki, and T. C. Poon, "Incoherent Digital Holography: A Review," *Appl. Sci.* **8**(1), 143 (2018). [CrossRef (<http://dx.doi.org/10.3390/app8010143>)] 
3. J. Rosen and G. Brooker, "Digital spatially incoherent correlation holography," *Opt. Lett.* **32**(8), 912–914 (2007). [CrossRef (<http://dx.doi.org/10.1364/OL.32.000912>)] 
4. T. L. Man, Y. H. Wan, W. J. Yan, X. H. Wang, E. J. G. Peterman, and D. Y. Wang, "Adaptive optics via self-interference digital holography for non-scanning three-dimensional imaging in biological samples," *Biomed. Opt. Express* **9**(6), 2614–2626 (2018). [CrossRef (<http://dx.doi.org/10.1364/BOE.9.002614>)] 
5. A. Marar and P. Kner, "Fundamental precision bounds for three-dimensional optical localization microscopy using self-interference digital holography," *Biomed. Opt. Express* **12**(1), 20–40 (2021). [CrossRef (<http://dx.doi.org/10.1364/BOE.400712>)] 
6. G. Pedrini, H. Li, A. Faridian, and W. Osten, "Digital holography of self-luminous objects by using a Mach-Zehnder setup," *Opt. Lett.* **37**(4), 713–715 (2012). [CrossRef (<http://dx.doi.org/10.1364/OL.37.000713>)] 
7. X. Y. Quan, M. Osamu, and A. Yasuhiro, "Single-shot incoherent digital holography using a dual-focusing lens with diffraction gratings," *Opt. Lett.* **42**(3), 383–386 (2017). [CrossRef (<http://dx.doi.org/10.1364/OL.42.000383>)] 
8. J. R. He, H. Ren, Y. Z. Tian, Q. X. Gong, Y. L. Du, X. M. Liu, C. X. Shan, J. P. Su, and F. Y. Ma, "Incoherent holographic camera based on Michelson interferometer," *J. Opt.* **21**(2), 025701 (2019). [CrossRef (<http://dx.doi.org/10.1088/2040-8986/aaf6de>)] 
9. W. Sheng, Y. W. Liu, Y. Y. Shi, H. C. Jin, and J. M. Wang, "Phase-difference imaging based on FINCH," *Opt. Lett.* **46**(11), 2766–2769 (2021). [CrossRef (<http://dx.doi.org/10.1364/OL.422038>)] 
10. C. M. Nguyen, M. Dilband, and K. Hyuk-Sang, "Spatially incoherent common-path off-axis color digital holography," *Appl. Opt.* **57**(6), 1504–1509 (2018). [CrossRef (<http://dx.doi.org/10.1364/AO.57.001504>)] 
11. A. Vijayakumar and J. Rosen, "Interferenceless coded aperture correlation holography—a new technique for recording incoherent digital holograms without two-wave interference," *Opt. Express* **25**(12), 13883–13896 (2017). [CrossRef (<http://dx.doi.org/10.1364/OE.25.013883>)] 
12. J. C. Wu, H. Zhang, W. H. Zhang, G. F. Jin, L. C. Cao, and G. Barbastathis, "Single-shot lensless imaging with fresnel zone aperture and incoherent illumination," *Light: Sci. Appl.* **9**(3), 563–573 (2020). [CrossRef (<http://dx.doi.org/10.1038/s41377-020-0289-9>)] 
13. J. Rosen and G. Brooker, "Non-scanning motionless fluorescence three-dimensional holographic microscopy," *Nat. Photonics* **2**(3), 190–195 (2008). [CrossRef (<http://dx.doi.org/10.1038/nphoton.2007.300>)] 

14. T. Yanagawa, R. Abe, and Y. Hayasaki, "Three-dimensional mapping of fluorescent nanoparticles using incoherent digital holography," *Opt. Lett.* **40**(14), 3312–3315 (2015). [CrossRef] (viewmedia.cfm?ur
Article Outline
15. C. Jang, J. Kim, D. C. Clark, B. Lee, and M. K. Kim, "Holographic fluorescence microscopy with incoherent digital holographic adaptive optics," *J. Biomed. Opt.* **20**(11), 111204 (2015). [CrossRef] "Investigation of the ef
Data Availability
16. J. Rosen and G. Brooker, "Fluorescence incoherent color holography," *Opt. Express* **15**(5), 2244–2250 (2007). [CrossRef (http://dx.doi.org/10.1364/OE.15.002244)] Equations (26)
References (34)
Cited By (1)
17. T. Hara, T. Tahara, Y. Ichihashi, R. Oi, and T. Ito, "Multiwavelength-multiplexed phase-shifting incoherent color digital holography," *Opt. Express* **28**(7), 10078–10089 (2020). [CrossRef] Metrics
Back to Top
18. M. K. Kim, "Adaptive optics by incoherent digital holography," *Opt. Lett.* **37**(13), 2694–2696 (2012). [CrossRef (http://dx.doi.org/10.1364/OL.37.002694)]
19. T. X. Xu, J. R. He, H. Ren, Z. C. Zhao, G. Q. Ma, Q. X. Gong, S. N. Yang, L. Dong, and F. Y. Ma, "Edge contrast enhancement of Fresnel incoherent correlation holography (FINCH) microscopy by spatial light modulator aided spiral phase modulation," *Opt. Express* **25**(23), 29207–29215 (2017). [CrossRef (http://dx.doi.org/10.1364/OE.25.029207)]
20. Y. Z. Bu, X. Wang, Y. Li, Y. L. Du, Q. X. Gong, G. C. Zheng, and F. Y. Ma, "Tunable edge enhancement by higher-order spiral Fresnel incoherent correlation holography system," *J. Phys. D: Appl. Phys.* **54**(12), 125103 (2021). [CrossRef (http://dx.doi.org/10.1088/1361-6463/abd12e)]
21. P. Bouchal, J. Kapitán, R. Chmelík, and Z. Bouchal, "Point spread function and two-point resolution in Fresnel incoherent correlation holography," *Opt. Express* **19**(16), 15603–15620 (2011). [CrossRef (http://dx.doi.org/10.1364/OE.19.015603)]
22. G. Indebetouw, E. M. Alouhab, and F. Richard, "Scanning holographic microscopy with transverse resolution exceeding the Rayleigh limit and extended depth of focus," *J. Opt. Soc. Am. A* **22**(5), 892–900 (2005). [CrossRef (http://dx.doi.org/10.1364/JOSAA.22.000892)]
23. J. Rosen, N. Siegel, and G. Brooker, "Theoretical and experimental demonstration of resolution beyond the Rayleigh limit by FINCH fluorescence microscopic imaging," *Opt. Express* **19**(27), 26249–26268 (2011). [CrossRef (http://dx.doi.org/10.1364/OE.19.026249)]
24. H. Ren, Y. Z. Bu, X. Wang, Y. Li, Y. L. Du, Q. X. Gong, J. H. Li, F. Y. Ma, and J. P. Su, "Incoherent digital holographic color imaging with high accuracy of image registration," *Infrared Laser Eng.* **49**(10), 227–232 (2020). [CrossRef (http://dx.doi.org/10.3788/IRLA20200022)]
25. M. T. Wu, Y. Zhang, M. Y. Tang, Z. Y. Duan, F. Y. Ma, Y. L. Du, E. J. Liang, and Q. X. Gong, "Two-step phase-shifting Fresnel incoherent correlation holography based on discrete wavelet transform," *Chin. Phys. B* **29**(12), 124201 (2020). [CrossRef (http://dx.doi.org/10.1088/1674-1056/abab7d)]

26. Y. Zhang, M. T. Wu, M. Y. Tang, F. Y. Ma, E. J. Liang, Y. L. Du, Z. Y. Duan, and Q. X. Gong, "Fresnel incoherent correlation hologram recording in real-time," *Opt. Express* **29**(16), 16693-166938 (2021). [CrossRef] (<http://dx.doi.org/10.1016/j.jlleo.2021.166938>)]
27. B. Katz and J. Rosen, "Super-resolution in incoherent optical imaging using synthetic aperture with Fresnel elements," *Opt. Express* **18**(2), 962-972 (2010). [CrossRef] (<http://dx.doi.org/10.1364/OE.18.000962>)]
28. B. Katz and J. Rosen, "Could SAFE concept be applied for designing a new Synthetic aperture telescope?" *Opt. Express* **19**(6), 4924-4936 (2011). [CrossRef] (<http://dx.doi.org/10.1364/OE.19.004924>)]
29. G. Brooker, N. Siegel, V. Wang, and J. Rosen, "Optimal resolution in Fresnel incoherent correlation holographic fluorescence microscopy," *Opt. Express* **19**(6), 5047-5062 (2011). [CrossRef] (<http://dx.doi.org/10.1364/OE.19.005047>)]
30. X. B. Chao, L. P. Pan, Z. S. Wang, F. T. Yang, and J. P. Ding, "Influence of pixelation effect of image sensor on resolution of Fresnel incoherent correlation holography," *Acta Phys. Sin.* **68**(6), 064203 (2019). [CrossRef] (<http://dx.doi.org/10.7498/aps.68.20181844>)]
31. B. Katz, J. Rosen, R. Kelner, and G. Brooker, "Enhanced resolution and throughput of Fresnel incoherent correlation holography (FINCH) using dual diffractive lenses on a spatial light modulator (SLM)," *Opt. Express* **20**(8), 9109-9121 (2012). [CrossRef] (<http://dx.doi.org/10.1364/OE.20.009109>)]
32. Y. Kashter, A. Vijayakumar, Y. Miyamoto, and J. Rosen, "Enhanced super resolution using Fresnel incoherent correlation holography with structured illumination," *Opt. Lett.* **41**(7), 1558-1561 (2016). [CrossRef] (<http://dx.doi.org/10.1364/OL.41.001558>)]
33. G. Brooker, N. Siegel, J. Rosen, N. Hashimoto, M. Kurihara, and A. Tanabe, "In-line FINCH super resolution digital holographic fluorescence microscopy using a high efficiency transmission liquid crystal GRIN lens," *Opt. Lett.* **38**(24), 5264-5267 (2013). [CrossRef] (<http://dx.doi.org/10.1364/OL.38.005264>)]
34. N. Siegel, J. Rosen, and G. Brooker, "Reconstruction of objects above and below the objective focal plane with dimensional fidelity by FINCH fluorescence microscopy," *Opt. Express* **20**(18), 19822-19835 (2012). [CrossRef] (<http://dx.doi.org/10.1364/OE.20.019822>)]

Article Outline

Figures (9)

Data Availability

Equations (26)

References (34)

Cited By (1)

Metrics

Back to Top

(viewmedia.cfm?ur

(mailto:?subject=Ar

Optics Express:%0AFer

"Investigation of the ef

31549-31560 (2021)%0

-----%0AThis i

99 ▾

◀ Previous Article (abstract.cfm?uri=oe-29-20-31537)

Next Article ▶ (abstract.cfm?uri=oe-29-20-31561)

Optics Express

James Leger, Editor-in-Chief

(/oe/home.cfm)

ABOUT (/OE/JOURNAL/OE/ABOUT.CFM)

ISSUES IN PROGRESS (/OE/UPCOMINGISSUE.CFM)

CURRENT ISSUE (/OE/ISSUE.CFM)

[ALL ISSUES \(/OE/BROWSE.CFM\)](/OE/BROWSE.CFM)

[FEATURE ISSUES \(/OE/FEATURE.CFM\)](/OE/FEATURE.CFM)

[Publishing Home \(/\)](#)

[Journals \(/about.cfm\)](/about.cfm)

[Conferences \(/conferences.cfm\)](/conferences.cfm)

INFORMATION FOR

[Authors \(/author/author.cfm\)](/author/author.cfm)

[Reviewers \(/reviewer/\)](/reviewer/)

[Librarians \(/library/\)](/library/)

OPEN ACCESS INFORMATION

[Open Access Statement and Policy \(/submit/review/open-access-policy-statement.cfm\)](/submit/review/open-access-policy-statement.cfm)

[Terms for Journal Article Reuse \(/library/license_v2.cfm\)](/library/license_v2.cfm)

OTHER RESOURCES

[Optica Publishing Group Bookshelf \(/books/default.cfm\)](/books/default.cfm)

[Industry Reports \(/industryreports.cfm\)](/industryreports.cfm)

[Optics & Photonics News ↗ \(https://www.optica-opn.org/home/\)](https://www.optica-opn.org/home/)

[Optics ImageBank ↗ \(https://imagebank.optica.org\)](https://imagebank.optica.org)

[Spotlight on Optics \(/spotlight/\)](/spotlight/)

ABOUT

[About Optica Publishing Group \(/about.cfm\)](/about.cfm)

[About My Account \(/benefitslog.cfm\)](/benefitslog.cfm)

[Contact Us \(/contactus.cfm\)](/contactus.cfm)

[Send Us Feedback](#)

[Optica Home \(https://www.optica.org\)](https://www.optica.org)  (HTTPS://WWW.TWITTER.COM/OPTICAPUBSGROUP) 

(HTTPS://WWW.FACEBOOK.COM/OPTICAWORLDWIDE) 

(HTTPS://WWW.LINKEDIN.COM/COMPANY/OPTICA-WORLDWIDE/)  (/TOC_ALERTS_SUBSCRIBE.CFM)

© Copyright 2022 | Optica Publishing Group. All Rights Reserved

[Privacy \(/privacy.cfm\)](/privacy.cfm) | [Terms of Use \(/termsofuse.cfm\)](/termsofuse.cfm)

Article Outline 

[Figures \(9\)](#)

[Data Availability](#)


[Equations \(26\)](#)


[References \(34\)](#)

[Cited By \(1\)](#)

[Metrics](#)

[Back to Top](#)

 [\(viewmedia.cfm?ur](#)

 [\(mailto:??subject=Ar](#)

[Optics Express:%0AFer](#)

["Investigation of the ef](#)

[31549-31560 \(2021\)%0](#)

[-----%0AThis i](#)

